sensors

MDPI

Article

A Novel Piezoresistive Accelerometer with SPBs to Improve the Tradeoff between the Sensitivity and the Resonant Frequency

Yu Xu †, Libo Zhao *,†, Zhuangde Jiang †, Jianjun Ding †, Niancai Peng † and Yulong Zhao †

State Key Laboratory for Manufacturing Systems Engineering, Collaborative Innovation Center of Suzhou Nano Science and Technology, Xi'an Jiaotong University, Xi'an 710049, China;
cactusxy@stu.xjtu.edu.cn (Y.X.); zdjiang@mail.xjtu.edu.cn (Z.J.); dingjianjun@126.com (J.D.);
ncpeng@mail.xjtu.edu.cn (N.P.); zhaoyulong@mail.xjtu.edu.cn (Y.Z.)
* Correspondence: libozhao@mail.xjtu.edu.cn; Tel.: +86-29-8266-8616
† These authors contributed equally to this work.

Academic Editor: Vittorio M.N. Passaro
Received: 6 December 2015; Accepted: 2 February 2016; Published: 6 February 2016

Abstract: For improving the tradeoff between the sensitivity and the resonant frequency of piezoresistive accelerometers, the dependency between the stress of the piezoresistor and the displacement of the structure is taken into consideration in this paper. In order to weaken the dependency, a novel structure with suspended piezoresistive beams (SPBs) is designed, and a theoretical model is established for calculating the location of SPBs, the stress of SPBs and the resonant frequency of the whole structure. Finite element method (FEM) simulations, comparative simulations and experiments are carried out to verify the good agreement with the theoretical model. It is demonstrated that increasing the sensitivity greatly without sacrificing the resonant frequency is possible in the piezoresistive accelerometer design. Therefore, the proposed structure with SPBs is potentially a novel option for improving the tradeoff between the sensitivity and the resonant frequency of piezoresistive accelerometers.

Keywords: piezoresistive accelerometer; sensitivity; resonant frequency; SPBs

1. Introduction

Vibration signals usually present different parameters, including velocity, displacement or acceleration, that can be measured by a velocity sensor, a displacement probe or an accelerometer, respectively. In practical applications, accelerometers is some of the most popular vibration sensors because of their convenience. When designing an accelerometer, the sensitivity and resonant frequency are often chosen as the most significant performance characteristics to optimize the structure. Due to the working principle based on the spring-mass system [1–3], the maximum displacement of the system is often regarded as an important manifestation of the accelerometer sensitivity. For example, piezoresistive or piezoelectric accelerometers count on the electrical variations caused by a stress, but the outputs in essence arise from the displacement of the spring-mass system [4–13]. In capacitive accelerometers, the output is directly affected by the displacement of the spring-mass system [14–16]. Therefore, there is a dependency between the displacement of the spring-mass system and the sensitivity of an accelerometer. The tradeoff between the displacement and resonant frequency of the spring-mass system is transformed into that between the sensitivity and resonant frequency of the accelerometer due to this dependency.

For improving the tradeoff between the resonant frequency and sensitivity in the accelerometer design, many studies have focused on new sensing mechanisms such as silicon nanowires in order

to obtain higher sensitivity [17–20]. However, these methods depend on new processes or new materials, and they are difficult to manufacture in mass production. Therefore, many researchers are still concentrated on the geometry design to optimize accelerometers [21–29].

In general, the product of the square of resonant frequency and the sensitivity is often chosen as a figure of merit (FOM) to evaluate the accelerometer performance [30]. The FOM can be expressed by the following equation:

$$\text{FOM} = S\omega^2 \tag{1}$$

where S is the sensitivity of the accelerometer, ω is the circular resonant frequency of the accelerometer. However, it is difficult to simultaneously increase the sensitivity and resonant frequency of an accelerometer.

In theory, the accelerometer detects the applied acceleration by using a proof mass based on the Newton's second law. Therefore, most accelerometers are designed as a second-order mass-spring-damper system, for which the following equation can be formulated:

$$ma_{applied} = m\ddot{x_o} + c\dot{x_o} + kx_o \tag{2}$$

where m is the mass of the proof mass, k is the spring constant, c is the damping ratio, $a_{applied}$ is the applied acceleration, and x_o is the displacement of the proof mass.

In the static response, the displacement of the proof mass is equivalent to the force generated by acceleration of the mass to the spring constant, an equation that can be expressed as:

$$x_o = \frac{ma_{applied}}{k} = \frac{a_{applied}}{\omega^2} \tag{3}$$

For the piezoresistive accelerometer, the sensitivity relies on the stress distribution of piezoresistors instead of the displacement of the accelerometer. Assuming a full Wheatstone bridge, the sensitivity of a piezoresistive accelerometer can be given by:

$$S = \frac{U_{out}}{a_{applied}} \frac{1}{U_{applied}} \tag{4}$$

where U_{out} is the output voltage and $U_{applied}$ is the applied voltage to the Wheatstone bridge. According to the working principle of the piezoresistive accelerometer, the output voltage is given by:

$$U_{out} = \pi\sigma U_{applied} \tag{5}$$

where π is the piezoresistive coefficient of the piezoresistors, σ presents the stress of the piezoresistors. They are both affected by the material property. From Equations (4) and (5), we can have:

$$S = \frac{\pi\sigma}{a_{applied}} \tag{6}$$

Therefore, Equations (1), (3) and (6) can be combined to:

$$\text{FOM} = S\frac{a_{applied}}{x_o} = \pi\frac{\sigma}{x_o} \tag{7}$$

Instead of increasing the sensitivity or resonant frequency individually in Equation (1), it is more reasonable to obtain a better stress per displacement ratio (denoted as σ/x_o) to improve FOM in Equation (7). However, in the conventional piezoresistive accelerometer shown in Figure 1, the piezoresistors are often embedded into a flexural component of the accelerometer such as a beam. The stress distribution of the piezoresistors usually depends on the displacement of the accelerometer under an applied acceleration, which indirectly results in a coupling relationship between x_o and S. Meanwhile, the dependency mentioned above can be also considered as the

dependency between x_o and σ. Therefore, it is difficult to weaken the dependency in conventional piezoresistive accelerometer designs.

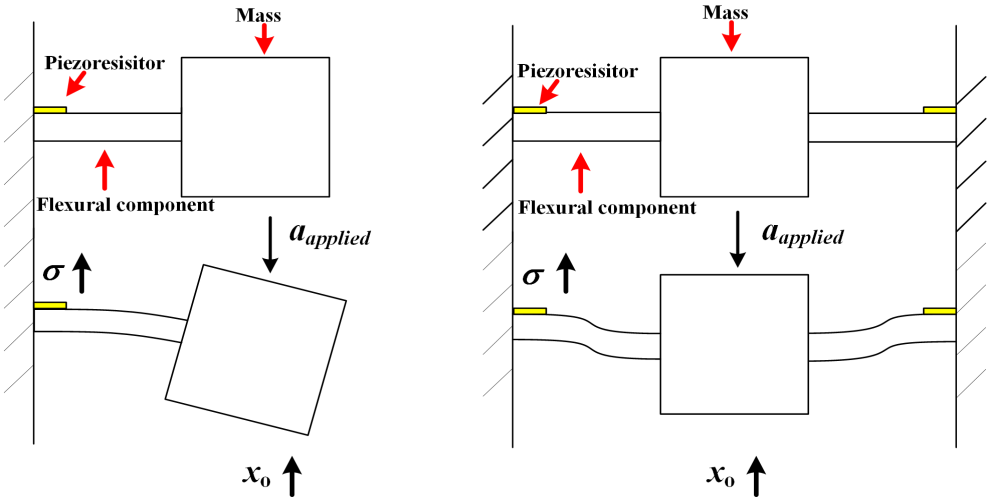

Figure 1. The dependency between x_o and σ in the conventional piezoresistive accelerometer.

In order to improve the tradeoff between the sensitivity and the resonant frequency, a novel structure with SPBs for the purpose of weakening the dependency between x_o and σ is proposed in this paper to optimize the performance of piezoresistive accelerometers. Firstly, a theoretical model based on the Euler-Bernoulli beam theory is derived. The theoretical formulas are also investigated to calculate the location of SPBs, the stress in SPBs and the resonant frequency of the structure. Secondly, the theoretical results are verified by finite element method (FEM) simulations. Meanwhile, the experimental results are also discussed to compare with the theoretical results and FEM results. Finally, the proposed structure is compared to that with same dimensions but without SPBs for further discussion.

2. Theory

2.1. Theoretical Structure

As shown in Figure 2, the schematic of the proposed structure consists with two masses, four SPBs ($b \times l \times h$) as the piezoresistors, two supporting beams ($w_1 \times L_1 \times T$) and one hinge ($w_2 \times L_2 \times T$). Each mass contains two balance masses ($e_1 \times d_1 \times T$) and one proof mass ($e_2 \times d_2 \times T$) which are considered as a rigid body. The SPB dimensions and d_{gap} are determined by the fabrication capability. Other parameters are determined by the SPB dimensions and measurement requirements including the measurement sensitivity and resonant frequency. Four SPBs are symmetrically located on two sides of the supporting beams to form the Wheatstone bridge for sensing acceleration.

Figure 3 shows the simplified structure of the proposed structure. When an acceleration is applied to the structure in the in-plane direction, both masses move upward and downward in parallel, and this results in a displacement of the supporting beams (denoted as Δy) and the rotations of the mass (denoted as θ). The stress distributions of the piezoresistors in the proposed structure should be a pure axial-deformation in order to avoid the stress losses to improve the sensitivity. The condition to achieve the pure axial-deformation of the SPBs depends on the distance (denoted as D) in y-axis from the center plane of the SPBs to that of the supporting beam. If the structure is properly designed, the y-direction displacement at the end of the SPBs can be offset by the rotation of the mass. Finally, only a pure axial-deformation (denoted as Δl) is generated in each SPB.

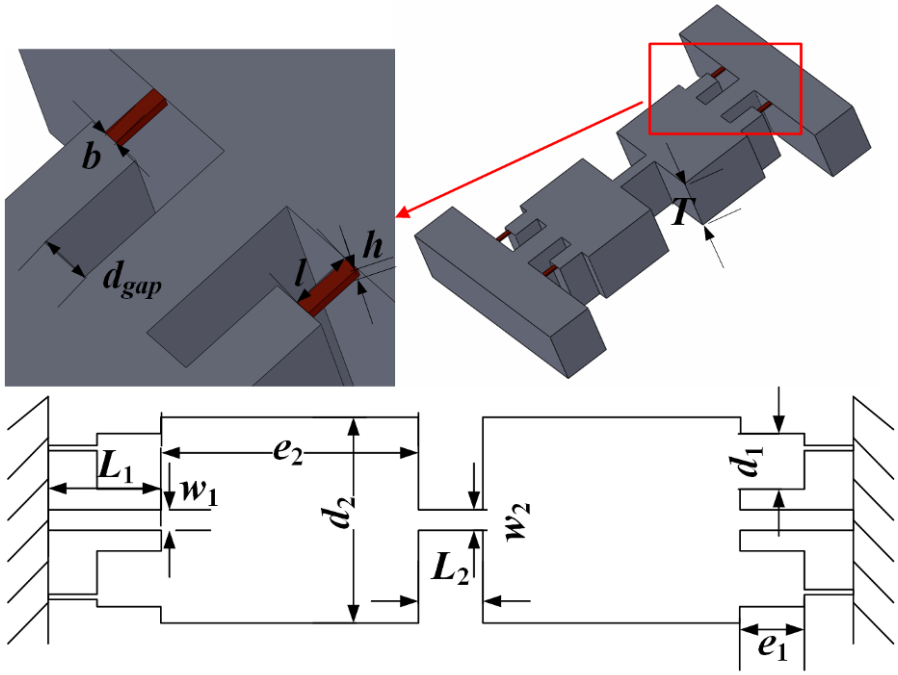

Figure 2. The schematic of the proposed structure.

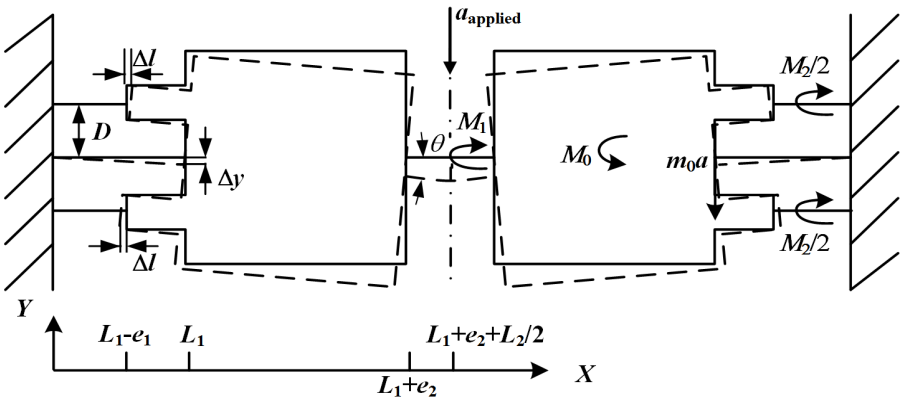

Figure 3. Simplified structure of the proposed structure.

Due to the axial symmetry of the proposed structure, only half of the structure is taken into considered in the analytical structure. Based on the Euler-Bernoulli beam theory and small deflection principle, when the acceleration is loaded to the structure in *y*-axis, the differential equations of force moment balance are expressed as:

$$EI_1Y_1''(x) = m_0(L_1 - x)a + M_0 - M_1 - M_2 \quad (0 < x < L_1) \tag{8}$$

$$EI_2Y_2''(x) = M_1 \quad (L_1 + e_2 < x < L_1 + e_2 + L_2/2) \tag{9}$$

The boundary conditions are:

$$Y_1(0) = 0 \tag{10}$$

$$Y_1'(0) = 0 \tag{11}$$

$$Y_1'(L_1) = Y_2''(L_1 + e_2) \tag{12}$$

$$Y_2'(L_1 + e_2 + L_2/2) = 0 \tag{13}$$

where E is Young's modulus of silicon. ρ is the density of silicon. $I_1 = {w_1}^3 T/12$ and $I_2 = {w_2}^3 T/12$ are the cross sectional moment of the supporting beam and the hinge, respectively. $Y_1(x)$ and $Y_2(x)$ are the displacements of the supporting beam and the hinge. m_0 is the total mass of one proof mass and two balance masses. M_0, M_1 and M_2 are the total inertial moment of the mass, the bending moment of the hinge and the restrictive moment of the SPBs, respectively.

The terms m_0, M_0 and M_1 can be expressed as:

$$m_0 = (2\rho e_1 d_1 T + \rho e_2 d_2 T) \tag{14}$$

$$M_0 = \left(\frac{1}{2}\rho e_2^2 d_2 T - \rho e_1^2 d_1 T\right) a \tag{15}$$

$$M_1 = \frac{I_2}{I_1 L_2/2 - I_2 L_1}\left(\frac{1}{2} m_0 L_1^2 a + M_0 L_1 - M_2 L_1\right) \tag{16}$$

When the SPBs achieve the pure axial-deformation, M_2 can be expressed as:

$$M_2 = 2FD = 2k_{\text{sensing}} \Delta l D = 2k_{\text{sensing}} D^2 \theta \tag{17}$$

where $\Delta l = D\theta$ is the pure axial-deformation of the SPBs. $F = k_{\text{sensing}}\ \Delta l$ is the axial force of the SPB and $k_{\text{sensing}} = Ebh/l$ is the spring constant of the SPB.

2.2. The Location of the SPBs for Achieving Axial-Deformation

Based on the theoretical structure mentioned above, θ can be calculated as:

$$\theta = \frac{a}{\dfrac{EI_1}{L_1} + \dfrac{EI_2}{L_2/2} + \dfrac{2Ebh}{l} D^2}\left(\frac{1}{2} m_0 L_1 + \frac{1}{2}\rho e_2^2 d_2 T - \rho e_1^2 d_1 T\right) \tag{18}$$

When the SPBs have achieved axial-deformation, the y-axis displacements of the SPBs ends connected with the balance mass should be zero. When $\theta << 1$ ($\theta \approx \tan\theta$), the y-axis displacement can be expressed as:

$$\Delta y_{\text{SPB}} = Y_1(L_1) - e_1\theta = \Delta y - e_1\theta = 0 \tag{19}$$

Therefore, θ can be also expressed as:

$$\theta = \frac{a}{\dfrac{EI_1 e_1}{L_1^2} + \dfrac{EI_2}{L_2} + \dfrac{Ebh}{l} D^2}\left(\frac{1}{3} m_0 L_1 + \frac{1}{4}\rho e_2^2 d_2 T - \frac{1}{2}\rho e_1^2 d_1 T\right) \tag{20}$$

From Equation (18) to Equation (20), the location of the SPBs can be expressed as:

$$\begin{aligned} D = \sqrt{\frac{l}{bh}\frac{1}{m_0}\frac{6}{L_1}} \times [&\left(\frac{I_1 e_1}{L_1^2} + \frac{I_2}{L_2}\right)\left(\frac{1}{2} m_0 L_1 + \frac{1}{2}\rho e_2^2 d_2 T - \rho e_1^2 d_1 T\right) - \\ &\left(\frac{I_1}{L_1} + \frac{I_2}{L_2/2}\right)\left(\frac{1}{3} m_0 L_1 + \frac{1}{4}\rho e_2^2 d_2 T - \frac{1}{2}\rho e_1^2 d_1 T\right)]^{\frac{1}{2}} \end{aligned} \tag{21}$$

As seen in Equation (21), it is clear that the location of the SPBs is only affected by the geometrical parameters and material density.

2.3. The Stress of the SPBs

After the location of the SPBs and θ are determined, it is easy to know the stress σ of the SPBs as:

$$\sigma = E\frac{\Delta l}{l} = E\frac{D\theta}{l} \tag{22}$$

Compared with other piezoresistive accelerometers, the stress of the SPBs depends not only on θ, which is directly proportional to the displacement of the structure (or, inversely proportion to the resonant frequency of the structure), but also the location of the SPBs.

2.4. The Frequency of the Structure

Based on the Rayleigh-Ritz method, the resonant frequency of the structure is calculated as:

$$f = \frac{1}{2\pi}\sqrt{\frac{\int_0^{L_1} EI_1[Y_1''(x)]^2dx + \int_{L_1+e_2}^{L_1+e_2+L_2/2} EI_2[Y_2''(x)]^2 + 2k_{\text{sensing}}\Delta l^2}{\int_{L_1}^{L_1+e_2} \rho d_2 t[Y_1(L_1) + Y_1'(L_1)\times(x-L_1)]^2dx + 2\int_{L_1-e_1}^{L_1} \rho d_1 t[Y_1(L_1) + Y_1'(L_1)\times(x-L_1)]^2dx}} \quad (23)$$

In Equation (23), the numerator consists of the elastic energies of the supporting beam, half the hinge and two SPBs. The denominator includes the kinetic energies of the proof mass and the two balance masses. From $\Delta l = D\theta$, it is clear that the resonant frequency of the structure is also influenced by the location of the SPBs.

3. Theoretical Validation

In this section, the validity and the accuracy of theoretical structure for calculating D with various geometrical parameters are discussed. Meanwhile, the effects of D on σ and f by geometry modification are presented. The simulations are carried out and compared with theoretical results by the commercial FEM software (ANSYS15.0, ANSYS Inc., Canonsburg, PA, USA). In all simulations, the applied acceleration and the material properties are kept with the same values. The applied acceleration is 100 g and the material properties include the density of 2330 kg/m^3, the elastic modulus of 170 GPa and the Poisson's ratio of v = 0.28. The values of T, b, h, l and d_{gap} are assumed to be constant. The initial geometrical dimensions are shown in Table 1.

Table 1. The initial geometrical dimensions.

	w_1	L_1	e_1	d_1	e_2	d_2	w_2	L_2	T	b	h	l	d_{gap}
Initial dimensions (μm)	70	500	430	395	1600	1000	30	500	310	5	10	70	70

3.1. The Effects of Various Geometrical Parameters on D

In this section, the accuracy of Equation (21) for calculating the locations of the SPBs with various geometrical dimensions is discussed. Figure 4 explains the influences of different geometrical parameters on D. The results demonstrate clearly that Equation (21) is remarkably precise for calculating D. The geometrical dimension ranges and maximum relative errors between the simulation and theoretical results are shown in Table 2.

Table 2. The geometrical dimension ranges and maximum relative errors.

	w_1	L_1	e_1	d_1
Geometrical dismension range (μm)	40–100	400–650	380–680	195–795
Max relative error	10.9%	9.4%	4.8%	5.1%
	e_2	d_2	w_2	L_2
Geometrical dismension range (μm)	1400–2000	800–1400	30–90	50–650
Max relative error	5.0%	4.5%	7.1%	4.6%

As shown in Figure 4a,b, it is clear that the value of D increases with an increasing w_1 or a decreasing L_1. In other word, the value of D increases with the enhancement of the supporting beam stiffness. It can be seen from Figure 4c,d that the value of D increases with an increasing e_1 or a decreasing d_1. Although it is difficult to summarize the effect of the balance mass, it is shown from the results that the balance mass still plays an important role in controlling D.

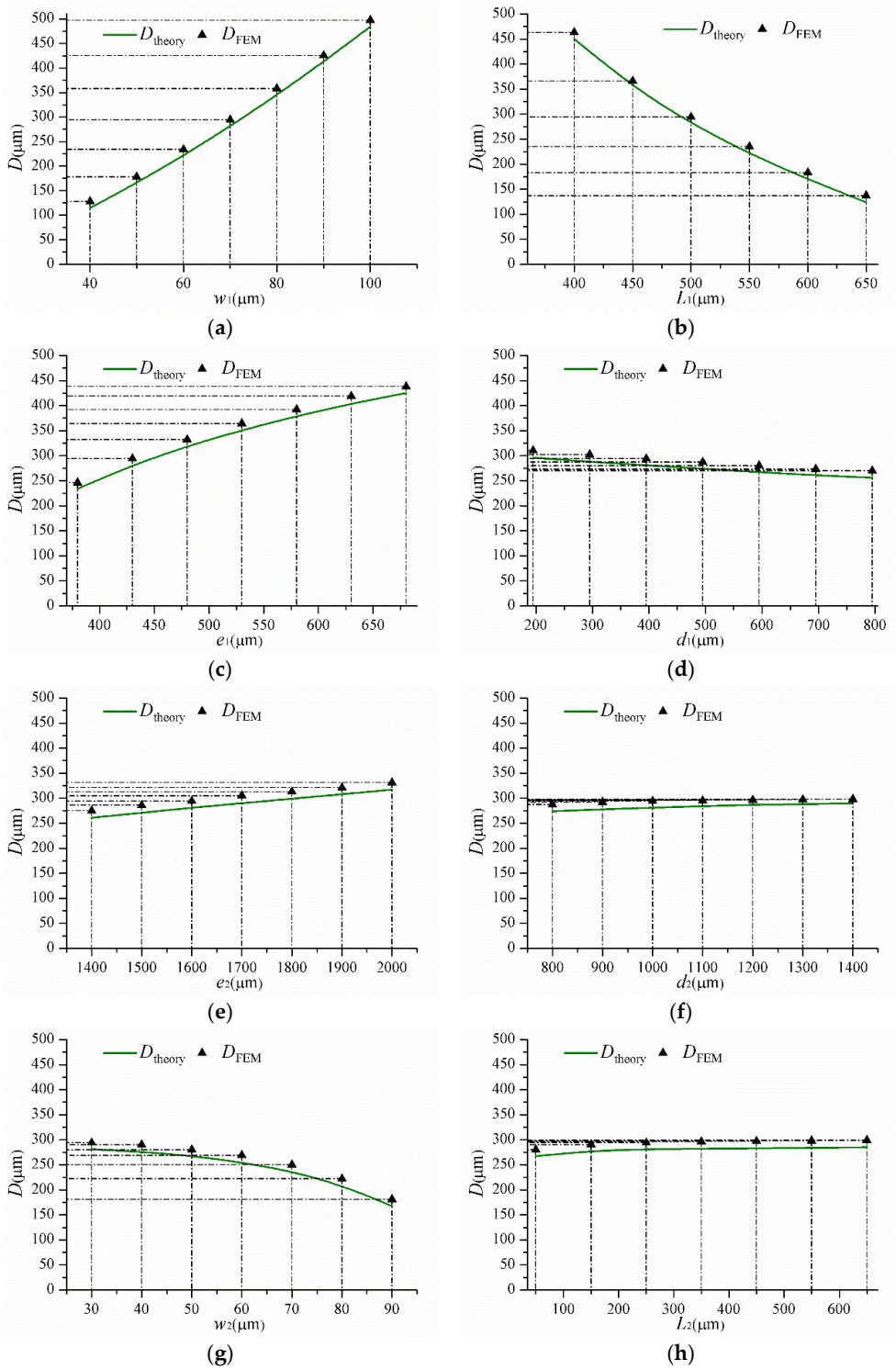

Figure 4. The effects of different geometrical parameters on D. (**a**) The effect of w_1; (**b**) The effect of L_1; (**c**) The effect of e_1; (**d**) The effect of d_1; (**e**) The effect of e_2; (**f**) The effect of d_2; (**g**) The effect of w_2; (**h**) The effect of L_2.

Figure 4e,f demonstrate the value of D increases with an increasing e_2 or an increasing d_2. Namely, D increases with the increasing weight of the proof mass. From Figure 4g,h, we can see that the value of D increases with a decreasing w_2 or an increasing L_2. In contrast to the supporting beam, D increases with decreasing the hinge stiffness in Figure 4g,h.

3.2. The Effects of Various Geometrical Parameters on σ and *f*

The influences of different geometrical parameters on σ and f are displayed in Figure 5. It is clearly demonstrated that Equations (22) and (23) are remarkably precise for calculating σ and f. The geometrical dimension ranges are the same as those in Table 2. The maximum relative errors between the simulation and theoretical results are shown in Table 3.

Table 3. The maximum relative errors.

	w_1	L_1	e_1	d_1	e_2	d_2	w_2	L_2
Maximum relative error of σ	10.3%	7.1%	8.3%	6.3%	6.7%	6.8%	9.4%	6.4%
Max relative error of f	8.0%	6.2%	3.7%	3.5%	3.2%	2.6%	2.9%	2.8%

The results indicate that the increasing stiffness of the supporting beam results in a decreasing σ or an increasing f in Figure 5a,b. In Figure 5c,d, a decreasing e_1 or an increasing d_1 led to an increasing σ and a decreasing f. The increasing weight of the proof mass results in an increasing σ and a decreasing f in Figure 5e,f. However, the results mentioned above show that the dependency between σ and f still exists. As shown in Figure 5g,h, with the dimensions of the hinge changed, the resonant frequency of the whole structure is affected a little but σ is still affected greatly when the dimensions of the hinge are changed. Comparing with other components, it shows a very different relationship between σ and f. It is easy to know that the increasing w_2 or decreasing L_2 results in the increasing stiffness of the hinge. Meanwhile, the increasing stiffness of the hinge leads to the decreasing D as shown in Figure 4g,h. The decreasing D makes the SPBs set less mechanical restrictions to the whole structure. The stiffening effect of the SPBs is decreased. Therefore, the stiffening effect between the hinge and the SPBs offsets each other. As a result, the resonant frequency of the whole structure is stabilized by the stiffening effect combined with both the hinge and the SPBs.

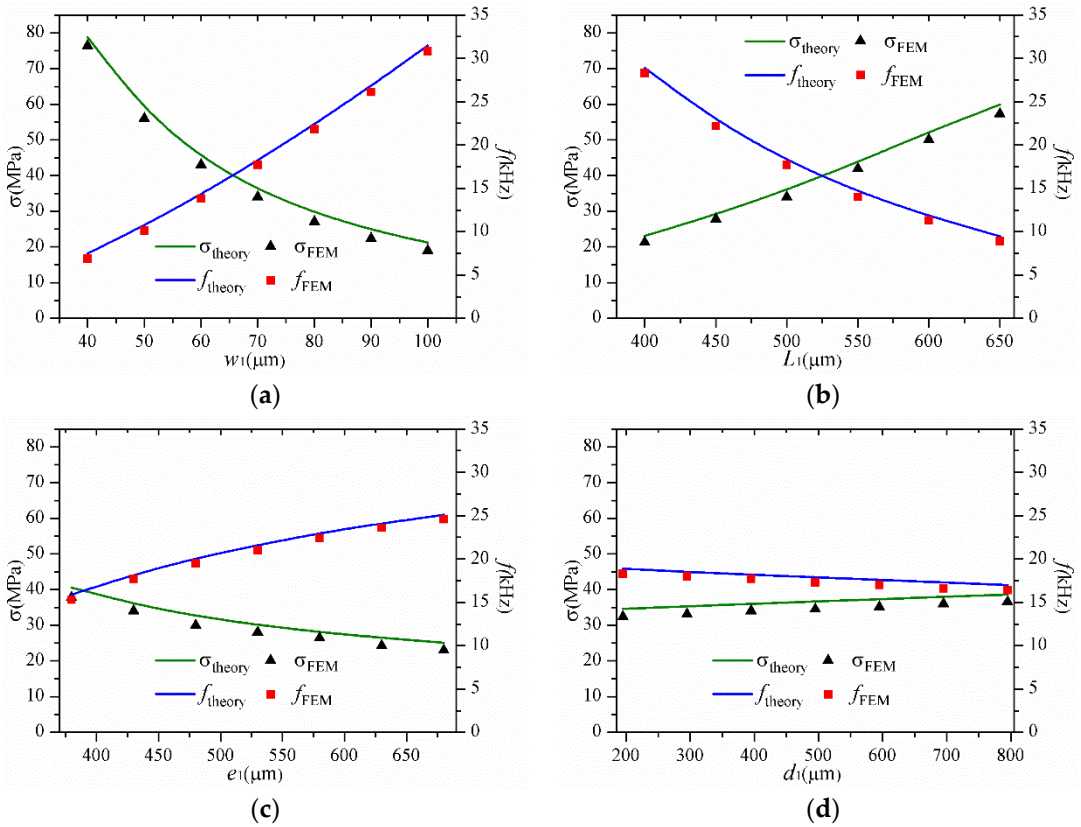

Figure 5. *Cont.*

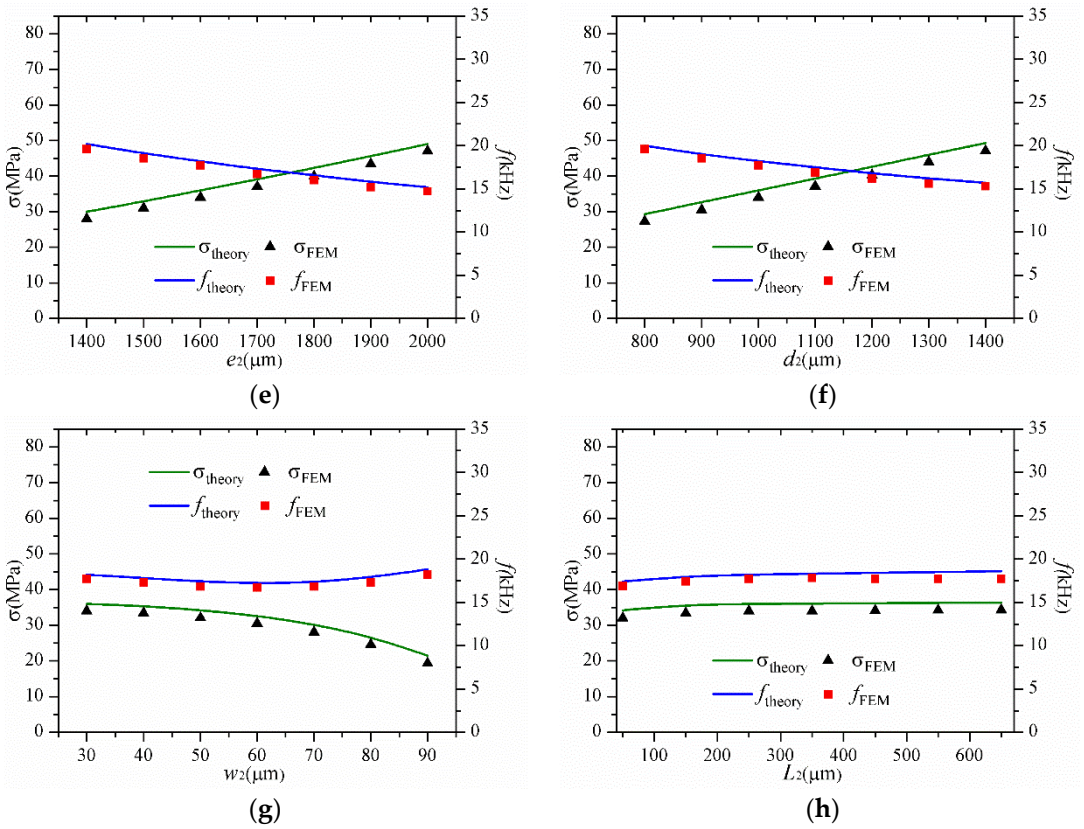

Figure 5. The effects of different geometrical parameters on σ and f. (**a**) The effect of w_1; (**b**) The effect of L_1; (**c**) The effect of e_1; (**d**) The effect of d_1; (**e**) The effect of e_2; (**f**) The effect of d_2; (**g**) The effect of w_2; (**h**) The effect of L_2.

From Equation (22), it is easy to know σ is affected by D and θ. θ is inversely proportional to the resonant frequency of the structure. It is clearly that σ is affected greatly by D when the resonant frequency of the whole structure is stabilized. In addition, σ is influenced rather more obviously by w_2 than L_2 because of the more effect of w_2 on D as shown in Figure 4g,h. In conclusion, the results show that the influences of the SPBs and the hinge play an important role in weakening the tradeoff between σ and f.

4. Results

In order to verify the results mentioned above, the proposed structure with SPBs is fabricated with a silicon-on-insulator (SOI) wafer using the micromachining fabrication process. The accelerometer chips are fabricated with three different w_2 values, including w_2 = 30 μm, w_2 = 70 μm and w_2 = 90 μm, respectively. Other dimensions are shown in Table 1. The main fabrication steps of the accelerometer are shown in Figure 6. The fabrication starts with the growth of silicon dioxide in the device layer. In next step, a 4 μm gap is etched at the back side of the wafer using inductively coupled plasma (ICP) technique to ensure the structure move freely after the bottom side is bonded to the Pyrex glass. Then, with the retained SiO_2 layer as a mask, the light boron is diffused to fabricate the piezoresistors. The nominal sheet resistance after drive-in technology approximates to 220 Ω/Y. After the light boron diffusion, the heavy boron diffusion is processed for ohmic contact. A 500 nm-thick Au layer is deposited onto the top surface of the wafer to complete metal electrodes after the contact holes are opened. The reactive ion etching (RIE) technology is processed from the front side to the BOX layer for shaping the SPBs. Then deep RIE (DRIE) is performed from the back side to the BOX layer for shaping the whole structure. Some details about RIE and DRIE are shown in Table 4. The BOX layer is wet etched to release the whole structure by buffered HF. At last, the Pyrex glass to the bottom of

the fabricated SOI wafer is packaged by the anodic bonding. Figure 7 shows the micrographs of the fabricated accelerometer chip.

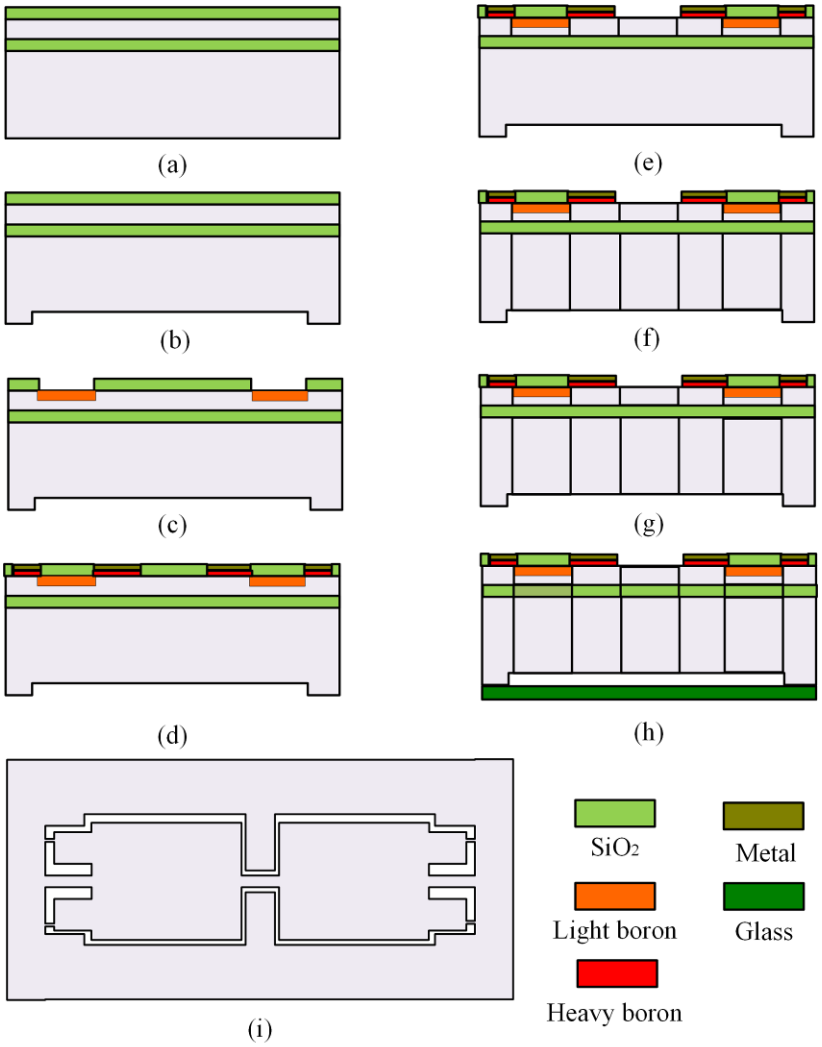

Figure 6. The fabrication process steps of the accelerometer. (**a**) Thermal oxidization; (**b**) ICP for the gap; (**c**) Light boron diffused for piezoresistors; (**d**) Heavy boron diffusion and metallization process; (**e**) RIE for front–side shape; (**f**) DRIE for back–side shape; (**g**) The BOX layer removed; (**h**) Anodic bonding between the SOI wafer and a Pyrex glass slide; (**i**) The top view of the chip.

Table 4. The details about RIE and DRIE process.

	Gas Flow (sccm)	RF Power (W)	Working Pressure (Pa)	Etching Rate (μm/min)
RIE	SF6:20	20	8	0.4
DRIE	SF_6:130 O_2:13 C_4F_8:85	Source power:1000 Bias power:20	5.7	4

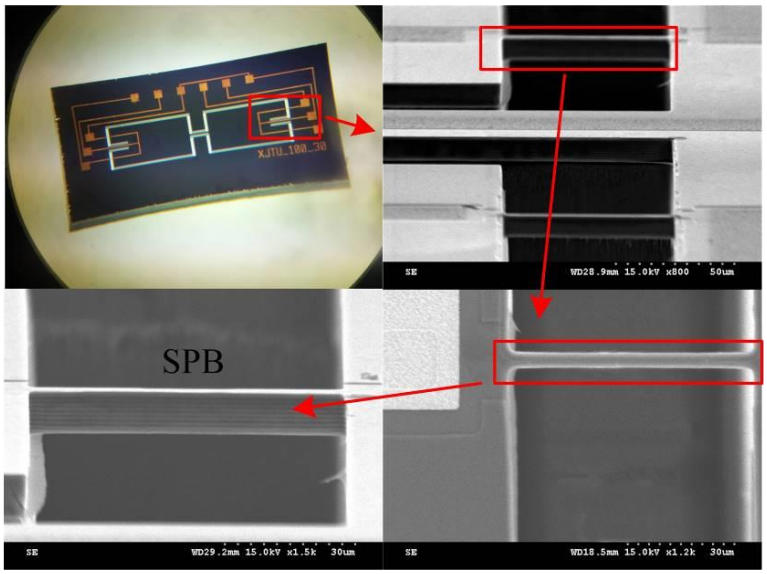

Figure 7. The micrograph of the fabricated chip.

The fabricated accelerometer chips are tested by static and dynamic experiments, respectively. The experimental setups are shown in Figure 8. First, a stable acceleration centrifugal machine (SY30-3, DONGLING, Suzhou, China) is used in static experiments for measuring the sensitivities of the different accelerometers.

Figure 8. The experiment setups (**a**) The static experiment (**b**) The dynamic experiment.

The full Wheatstone bridge integrated in each accelerometer is powered with DC 3 V. For safety reasons, the measured range in the static experiments is from 0 to 30 g. Figure 9 shows the output voltages *versus* the accelerations, and then the sensitivities are calculated. Next, the dynamic experiments are investigated by a set of calibration system including a data acquisition system (LMS

SCADAS305, Siemens, Munich, Germany), a power amplifier (MB500VI, MB Dynamics, Cleveland, OH, USA), and a vibration exciter (MODAL 110, MB Dynamics, Cleveland, OH, USA). When the swept-frequency of the sinusoidal signal is close to the resonant frequencies of different accelerometers, then the peaks of the dynamic response curves are related to the resonant frequencies. The dynamic curves of the output voltage ratios *versus* different frequencies are shown in Figure 10. The measuring sensitivities and the resonant frequencies are obtained in the Table 5. Based on the experimental results, these accelerometers have different sensitivities, but nearly the same resonant frequencies. The results show a good agreement with the theoretic and FEM results. Therefore, the proposed novel structure is verified as an excellent solution to weaken the tradeoff between the sensitivity and resonant frequency.

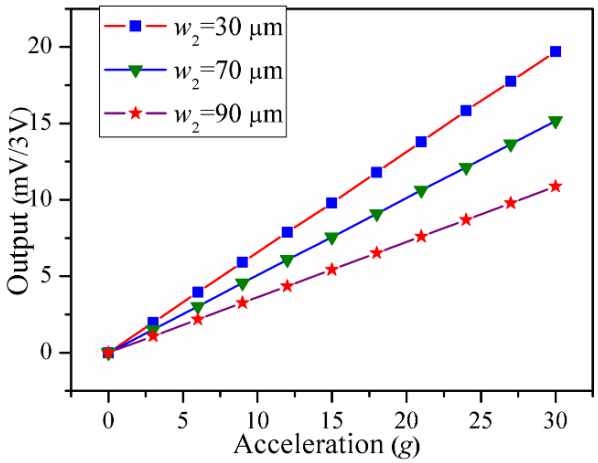

Figure 9. The output voltages *versus* the accelerations.

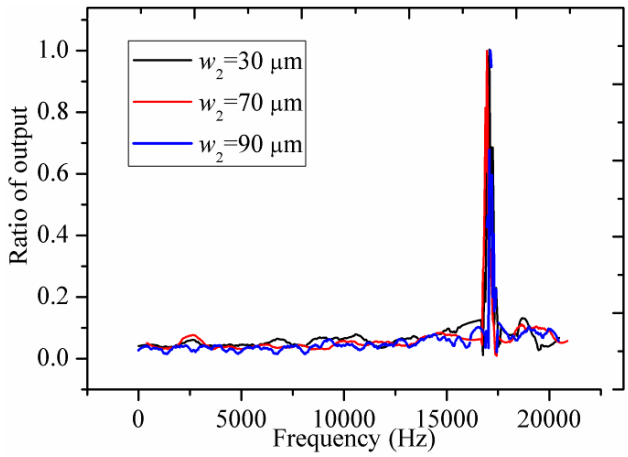

Figure 10. The dynamic curves of output voltage ratios *versus* different frequencies.

Table 5. The measuring sensitivities and the resonant frequencies.

	w_2 = 30 μm	w_2 = 70 μm	w_2 = 90 μm
Measuring sensitivity (mV/g/3V)	0.666	0.505	0.363
Resonant frequency (kHz)	17.1	16.9	17.2

5. Discussion

In order to further obtain the influences of the combined stiffening effect on stabilizing the resonant frequency, a similar structure without SPBs is shown in Figure 11. In general, the maximum displacement of the structure is inversely proportion to the resonant frequency of the structure.

Therefore, the maximum displacement and the resonant frequency of the structure are examined in FEM simulations. The initial dimensions are given in Table 1. The comparisons of the maximum displacement and the resonant frequency of the proposed structure without the SPBs are illustrated in Figure 12, respectively. Like most conventional piezoresistive accelerometer structures, the maximum displacement decreases with the increasing resonant frequency. However, as shown in Figure 13, the displacement and resonant frequency of the proposed structure with SPBs, show little change in a certain range with the variation of w_2 or L_2.

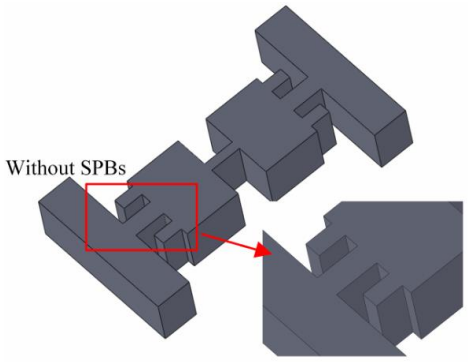

Figure 11. The structure without SPBs.

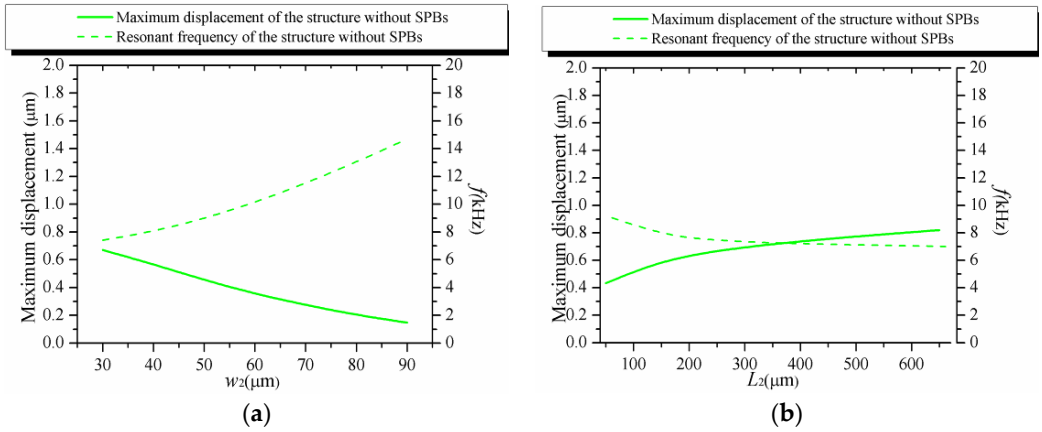

Figure 12. The maximum displacement and the resonant frequency of the structure without the SPBs. (**a**) The effect of w_2; (**b**) The effect of L_2.

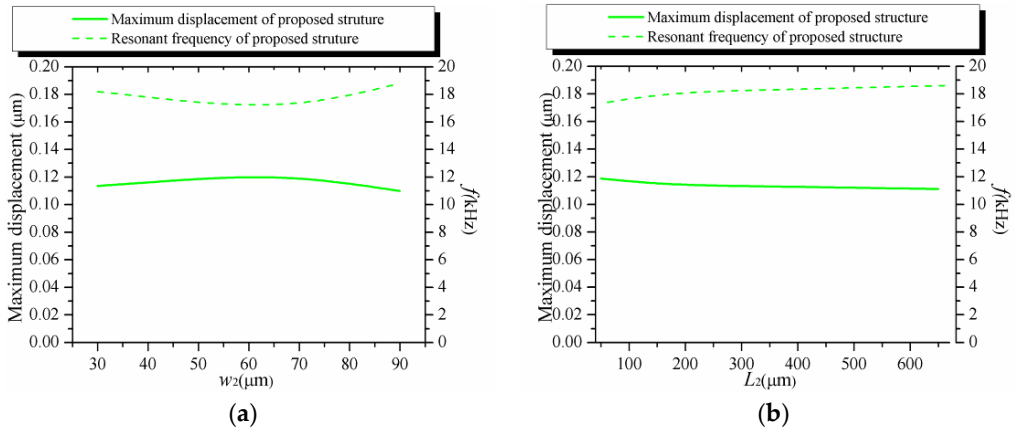

Figure 13. The maximum displacement and the resonant frequency of our proposed structure. (**a**) The effect of w_2; (**b**) The effect of L_2.

Considering the results illustrated in Figures 12 and 13 the combined stiffening effect between the SPBs and the hinge plays an important role in stabilizing the maximum displacement and the resonant frequency. Combined with the results mentioned above, it is demonstrated that the dependence between the displacement and the sensitivity of accelerometer is weakened by our proposed structure.

6. Conclusions

For improving the tradeoff between the sensitivity and the resonant frequency, a novel structure with SPBs is proposed for weakening the dependency between the displacement and σ in accelerometer design. FEM simulations, comparative simulations and experiments are carried out to verify the theoretical model, with good agreement. The theoretical and FEM results show that the stress of the piezoresistor increases without sacrificing the resonant frequency when w_2 and L_2 are changed. The experimental results show that the accelerometers fabricated with different w_2 values have significant differences in the sensitivities from 0.363 mV/g/3 V to 0.666 mV/g/3 V but differences of the resonant frequencies from 16.9 kHz to 17.2 kHz are not as evident. It is shown that the tradeoff between the sensitivity and the resonant frequency is changed by the stiffening effect combined with the hinge and the SPBs. In order to further discuss the combined stiffening effect, a similar structure without SPBs is compared with the proposed structure. The comparisons demonstrate that the combined stiffening effect between the SPBs and the hinge plays an indispensable role in weakening the dependence mentioned above. Above all, the proposed structure with SPBs is potentially a better approach for improving the tradeoff between the sensitivity and the resonant frequency to guarantee the high performance of piezoresistive accelerometers.

Acknowledgments: This work was supported in part by the National Key Scientific Instrument and Equipment Development Projects of China (2012YQ03026101), the National Natural Science Foundation of China (51375378, 51205306, 91323303), the Fundamental Research Funds for the Central Universities (2012jdgz08), the Major National Science and Technology Project (2011ZX04004-061), and the 111 Program (B12016).

Author Contributions: Yu Xu and Libo Zhao conceived and designed the experiments. Zhuangde Jiang contributed reagents/materials/analysis tools. Jianjun Ding performed the experiments. Yulong Zhao and Niancai Peng analyzed the data. Yu Xu wrote the paper.

Conflicts of Interest: The authors declare no conflict of interest.

References

1. Bao, M.-H. *Micro Mechanical Transducers: Pressure Sensors, Accelerometers and Gyroscopes*; Elsevier: Amsterdam, The Netherlands, 2000; Volume 3, pp. 247–250.
2. Mukhiya, R.; Gopal, R.; Pant, B.D.; Khanna, V.K.; Bhattacharyya, T.K. Design, modeling and fem-based simulations of a 1-dof mems bulk micromachined piezoresistive accelerometer. *Microsyst. Technol.* **2014**, *21*, 2241–2258. [CrossRef]
3. Kraft, M. Micromachined inertial sensors: State-of-the-art and a look into the future. *Meas. Control* **2000**, *33*, 164–168. [CrossRef]
4. Kobayashi, T.; Okada, H.; Masuda, T.; Maeda, R.; Itoh, T. A digital output accelerometer using mems-based piezoelectric accelerometer connected to parallel CMOS circuit. *Procedia Eng.* **2010**, *5*, 1071–1074. [CrossRef]
5. Zheng, Q.; Xu, Y. Asymmetric air-spaced cantilevers for vibration energy harvesting. *Smart Mater. Struct.* **2008**, *17*, 6777–6790. [CrossRef]
6. Kovács, Á.; VíZváry, Z. Structural parameter sensitivity analysis of cantilever and bridge-type accelerometers. *Sens. Actuators A Phys.* **2001**, *89*, 197–205. [CrossRef]
7. Nemirovsky, Y.; Nemirovsky, A.; Muralt, P.; Setter, N. Design of novel thin-film piezoelectric accelerometer. *Sens. Actuators A Phys.* **1996**, *56*, 239–249. [CrossRef]
8. Han, G.Y.; Zou, L.; Deng, K.; Wolf, R.; Tadigadapa, S.; Trolier-Mckinstry, S. Lead zirconate titanate MEMS accelerometer using interdigitated electrodes. *Sens. Actuators A Phys.* **2003**, *107*, 26–35.
9. Roylance, L.M.; Angell, J.B. A batch-fabricated silicon accelerometer. *IEEE Trans. Electron Dev.* **1980**, *26*, 1911–1917. [CrossRef]

10. Wei, C.; Zhou, W.; Wang, Q.; Xia, X.; Li, X. Tpms (tire-pressure monitoring system) sensors: Monolithic integration of surface-micromachined piezoresistive pressure sensor and self-testable accelerometer. *Microelectron. Eng.* **2012**, *91*, 167–173. [CrossRef]
11. Zhao, Y.; Sun, L.; Liu, Y.; Wang, W.; Tian, B. Incorporation of the stress concentration slots into the flexures for a high-performance microaccelerometer. *Rev. Sci. Instrum.* **2012**, *83*. [CrossRef] [PubMed]
12. Sankar, A.R.; Das, S.; Lahiri, S.K. Cross-axis sensitivity reduction of a silicon MEMS piezoresistive accelerometer. *Microsyst. Technol.* **2009**, *15*, 511–518. [CrossRef]
13. Liu, J.; Shi, Y.; Li, P.; Tang, J.; Zhao, R.; Zhang, H. Experimental study on the package of high-g accelerometer. *Sens. Actuators A Phys.* **2012**, *173*, 1–8. [CrossRef]
14. Farahani, H.; Mills, J.K.; Cleghorn, W.L. Design, fabrication and analysis of micromachined high sensitivity and 0% cross-axis sensitivity capacitive accelerometers. *Microsyst. Technol.* **2009**, *15*, 1815–1826. [CrossRef]
15. Yu, J.C.; Lee, C.; Kuo, W.; Chang, C. Modeling analysis of a triaxial microaccelerometer with piezoelectric thin-film sensing using energy method. *Microsyst. Technol.* **2011**, *17*, 483–493. [CrossRef]
16. Zhou, X.; Che, L.; Liang, S.; Lin, Y.; Li, X.; Wang, Y. Design and fabrication of a MEMS capacitive accelerometer with fully symmetrical double-sided h-shaped beam structure. *Microelectron. Eng.* **2015**, *131*, 51–57. [CrossRef]
17. Mehran, M.; Mohajerzadeh, S. High sensitivity nanostructure incorporated interdigital silicon based capacitive accelerometer. *Microelectr. J.* **2015**, *46*, 166–173. [CrossRef]
18. Toriyama, T.; Tanimoto, Y.; Sugiyama, S. Single crystal silicon nano-wire piezoresistors for mechanical sensors. *J. Microelectromech. Syst.* **2002**, *11*, 605–611. [CrossRef]
19. Dao, D.V.; Toriyama, T.; Sugiyama, S. Noise and frequency analyses of a miniaturized 3-dof accelerometer utilizing silicon nanowire piezoresistors. In Proceedings of the 2004 IEEE Sensors, Vienna, Austria, 24–27 October 2004; pp. 1464–1467.
20. Amarasinghe, R.; Dao, D.V.; Toriyama, T.; Sugiyama, S. Development of miniaturized 6-axis accelerometer utilizing piezoresistive sensing elements. *Sens. Actuators A Phys.* **2007**, *134*, 310–320. [CrossRef]
21. Roy, A.L.; Bhattacharyya, T.K. Design, fabrication and characterization of high performance SOI MEMS piezoresistive accelerometers. *Microsyst. Technol.* **2013**, *21*, 55–63. [CrossRef]
22. Perez, M.; Eklund, E.J.; Shkel, A.M. Designing micromachined accelerometers with interferometric detection. In Proceedings of the 2005 IEEE Sensors, Irvine, CA, USA, 30 October–3 November 2005; pp. 652–655.
23. Khir, M.H.M.; Peng, Q.; Hongwei, Q. A low-cost COMS-MEMS piezoresistive accelerometer with large proof mass. *Sensors* **2011**, *11*, 7892–7907. [CrossRef] [PubMed]
24. Wang, J.; Li, X. A high-performance dual-cantilever high-shock accelerometer single-sided micromachined in (111) silicon wafers. *J. Microelectromech. Syst.* **2011**, *19*, 1515–1520. [CrossRef]
25. Wung, T.S.; Ning, Y.T.; Chang, K.H.; Tang, S.; Tsai, Y.X. Vertical-plate-type microaccelerometer with high linearity and lowcross-axis sensitivity. *Sens. Actuators A Phys.* **2015**, *222*, 284–292. [CrossRef]
26. Lim, M.K.; Du, H.; Su, C.; Jin, W.L. A micromachined piezoresistive accelerometer with high sensitivity: Design and modelling. *Microelectron. Eng.* **1999**, *49*, 263–272. [CrossRef]
27. Huang, S.; Li, X.; Song, Z.; Wang, Y.; Yang, H.; Che, L.; Jiao, J. A high-performance micromachined piezoresistive accelerometer with axially stressed tiny beams. *J. Micromech. Microeng.* **2005**, *15*, 993–1000. [CrossRef]
28. Dong, P.; Li, X.; Yang, H.; Bao, H.; Zhou, W.; Li, S.; Feng, S. High-performance monolithic triaxial piezoresistive shock accelerometers. *Sens. Actuators A Phys.* **2008**, *141*, 339–346. [CrossRef]
29. Kuells, R.; Nau, S.; Salk, M.; Thoma, K. Novel piezoresistive high-g accelerometer geometry with very high sensitivity-bandwidth product. *Sens. Actuators A Phys.* **2012**, *182*, 41–48. [CrossRef]
30. Seidel, H.; Csepregi, L. Design optimization for cantilever-type accelerometers. *Sens. Actuators A Phys.* **1984**, *6*, 81–92. [CrossRef]